LETTER

https://doi.org/10.1038/s41586-018-0209-9

Structural basis of G-quadruplex unfolding by the DEAH/RHA helicase DHX36

Michael C. Chen[1,2], Ramreddy Tippana[3], Natalia A. Demeshkina[1], Pierre Murat[2], Shankar Balasubramanian[2,4], Sua Myong[3] & Adrian R. Ferré-D'Amaré[1]*

Guanine-rich nucleic acid sequences challenge the replication, transcription, and translation machinery by spontaneously folding into G-quadruplexes, the unfolding of which requires forces greater than most polymerases can exert[1,2]. Eukaryotic cells contain numerous helicases that can unfold G-quadruplexes[3]. The molecular basis of the recognition and unfolding of G-quadruplexes by helicases remains poorly understood. DHX36 (also known as RHAU and G4R1), a member of the DEAH/RHA family of helicases, binds both DNA and RNA G-quadruplexes with extremely high affinity[4–6], is consistently found bound to G-quadruplexes in cells[7,8], and is a major source of G-quadruplex unfolding activity in HeLa cell lysates[6]. DHX36 is a multi-functional helicase that has been implicated in G-quadruplex-mediated transcriptional and post-transcriptional regulation, and is essential for heart development, haematopoiesis, and embryogenesis in mice[9–12]. Here we report the co-crystal structure of bovine DHX36 bound to a DNA with a G-quadruplex and a 3′ single-stranded DNA segment. We show that the N-terminal DHX36-specific motif folds into a DNA-binding-induced α-helix that, together with the OB-fold-like subdomain, selectively binds parallel G-quadruplexes. Comparison with unliganded and ATP-analogue-bound DHX36 structures, together with single-molecule fluorescence resonance energy transfer (FRET) analysis, suggests that G-quadruplex binding alone induces rearrangements of the helicase core; by pulling on the single-stranded DNA tail, these rearrangements drive G-quadruplex unfolding one residue at a time.

DEAH/RHA helicases share a structural core[13–18] consisting of two RecA-like domains (RecA1 and RecA2) followed by a C-terminal domain (itself comprised of degenerate-winged-helix (WH), ratchet-like (RL), and oligonucleotide and oligosaccharide-binding-fold-like (OB) subdomains). At its N terminus, DHX36 augments the DEAH/RHA core with a glycine-rich element followed by the DHX36-specific motif (DSM; Fig. 1a, Extended Data Fig. 1). The DSM is essential for binding of DHX36 to G-quadruplexes[19]. We

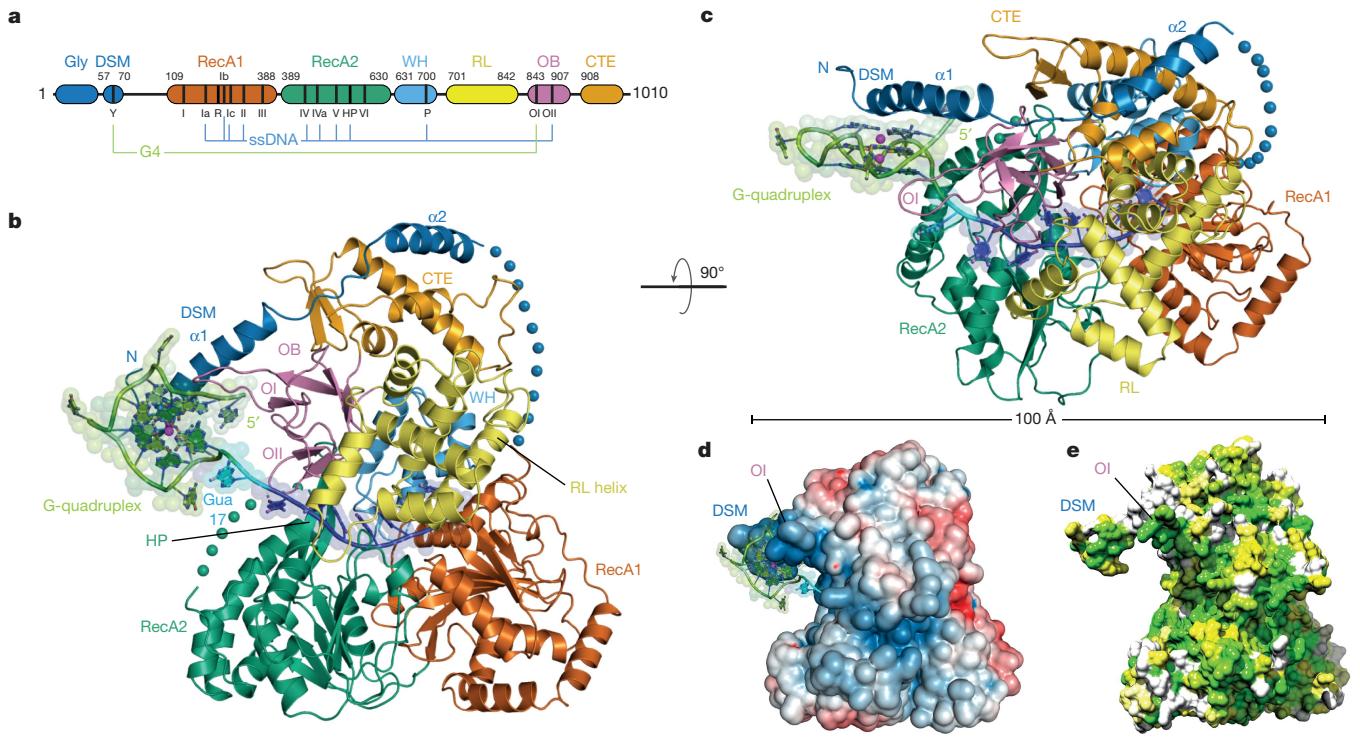

Fig. 1 | Overall structure of the DHX36–G-quadruplex DNA complex. **a**, Domain organization; G-quadruplex (G4)- and ssDNA-interacting regions indicated. **b**, Cartoon representation of the co-crystal structure of DHX36 bound to DNA^{Myc}, colour-coded as in **a**. Spheres denote two disordered segments (blue, 20 and 53 residues in the crystallization construct and wild-type, respectively; green, 13 residues). OB loops I and II (OI and OII) contact DNA. **c**, As in **b**, rotated by 90°. **d**, Electrostatic potential calculated with DNA omitted from the co-crystal structure (blue to red, ±5 k_BT). **e**, Phylogenetic conservation among 250 DHX36 orthologues (white to green, least to most conserved).

[1]Biochemistry and Biophysics Center, National Heart, Lung and Blood Institute, Bethesda, MD, USA. [2]Department of Chemistry, University of Cambridge, Cambridge, UK. [3]Biophysics Department, Johns Hopkins University, Baltimore, MD, USA. [4]Cancer Research UK Cambridge Institute, University of Cambridge, Cambridge, UK. *e-mail: adrian.ferre@nih.gov

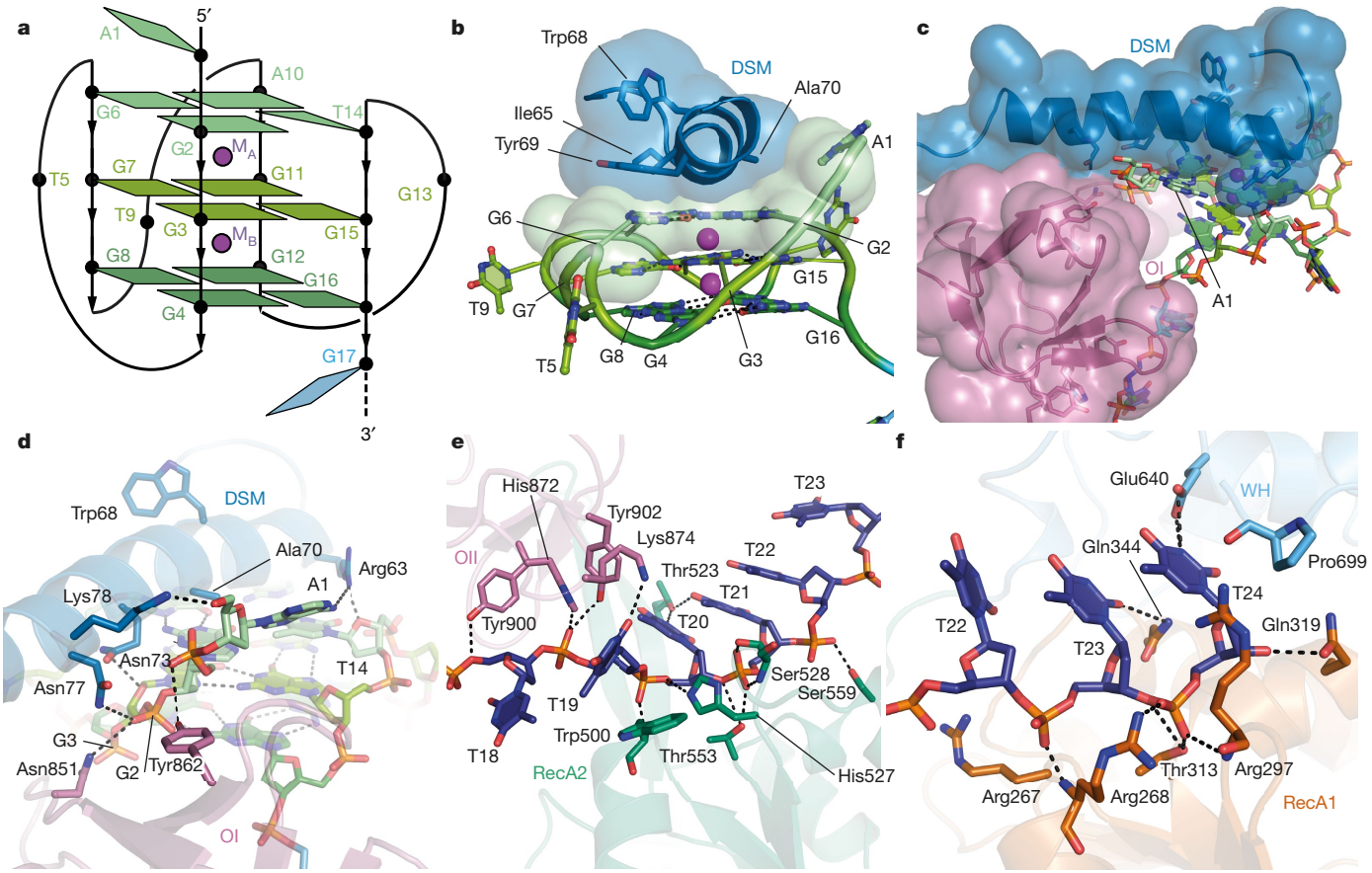

Fig. 2 | DHX36–DNA interaction. a, Schematic of the DHX36-bound all-parallel G-quadruplex. **b**, The DSM stacks on the 5′ (top) non-canonical quartet. Transparent spheres represent van der Waals radii. **c**, The DSM and the OI loop of the OB domain flank A1. **d**, Interaction of the DSM and loop OI of DHX36 with the DNA backbone near the 5′ end of DNA^{Myc}. **e**, Interaction of the OII loop and the RecA2 domain with T18–T22 of the 3′ single-stranded region of DNA^{Myc}. **f**, Interaction of the RecA1 and WH domains of DHX36 with T23–T24 of the 3′ single-stranded region of DNA^{Myc}.

co-crystallized a DHX36 construct missing the glycine-rich element but containing the full DSM (hereafter DHX36-DSM; this construct has G-quadruplex binding and repetitive unfolding activity comparable to those of wild-type bovine and human DHX36, Extended Data Fig. 2) with a 24-nucleotide (nt) DNA (hereafter, DNA^{Myc}) comprised of a *Myc*-promoter-derived G-quadruplex-forming sequence[20] followed by a 3′ single-stranded extension of seven thymidines. We also crystallized a truncated DHX36 without the glycine-rich and DSM elements (hereafter, DHX36-core). Structures were solved through the single-wavelength anomalous dispersion (SAD) and molecular replacement methods (Extended Data Tables 1, 2, Extended Data Fig. 3; see Methods).

In the DHX36-DSM–DNA^{Myc} complex, the RecA1, RecA2, and C-terminal domains are arranged as a trefoil (Fig. 1b). Connected to RecA1 by a disordered linker, the N-terminal extension folds into two α-helices, the first of which contains the DSM. This DSM helix projects away from the body of the helicase and contacts the 5′ (top) face of the bound G-quadruplex (Fig. 1c). The OB domain contacts both the G-quadruplex and the adjacent single-stranded segment of DNA^{Myc}, the 3′-side of which is held in a nucleic-acid-binding channel formed by the RecA1, RecA2, and C-terminal domains. The amphipathic DSM helix is overall cationic, and the path of the single-stranded DNA follows a positively charged groove between the RecA2 and C-terminal domains (Fig. 1d). This groove is too narrow to accommodate double-stranded DNA, consistent with the requirement[6,21–23] for a 3′ single-stranded extension for DHX36 activity. Phylogenetic conservation largely follows this groove and extends to the non-polar face of the DSM helix (Fig. 1e).

Solution NMR has shown[20,24] that residues 1–17 of DNA^{Myc} fold into a stable, parallel, three-tiered G-quadruplex (Extended Data Fig. 4a, b). Our co-crystal structure reveals that association with the helicase reorganizes the DNA. Instead of three canonical G-quartets, the DHX36-bound DNA contains two G-quartets stacked underneath a non-canonical A•T•G•G quartet. The top G-quartet is absent because G17, which was the 3′-most guanine of the bottom G-quartet[20], has been pulled by the helicase into the 3′ single-stranded region. Shifting the DNA sequence by one residue while maintaining an overall three-tiered G-quadruplex structure with minimal propeller loops forces a new A10•T14 Watson–Crick pair to form the top quartet together with G2 and G6 (Fig. 2a, Extended Data Fig. 4b). The DHX36-bound rearranged G-quadruplex is considerably less stable than the free, canonical *Myc* G-quadruplex (Extended Data Fig. 5), indicative of the degree of destabilization caused by DHX36 binding alone.

The DSM has been shown[19] to be necessary but not sufficient for high-affinity G-quadruplex binding by DHX36; the full-length helicase and an isolated DSM peptide bind to G-quadruplexes with dissociation constants of below 10 pM and 310 nM, respectively[4,12,19]. This is consistent with the helicase core contributing to the DHX36–DNA interface (Fig. 1b, c). In the co-crystal structure, a hydrophobic core is formed by the α-helical DSM residues Ile65, Trp68, Tyr69 and Ala70, producing a flat non-polar surface that stacks on the nucleobases of the top quartet of the bound G-quadruplex (Fig. 2b), reminiscent of the mode of G-quadruplex recognition by planar small molecules[25]. The single-stranded A1, which is 5′ to the G-quadruplex in our structure, packs between the α1 DSM helix and the OB domain (Fig. 2c). The C-terminal side of the α1 DSM helix and the first loop of the

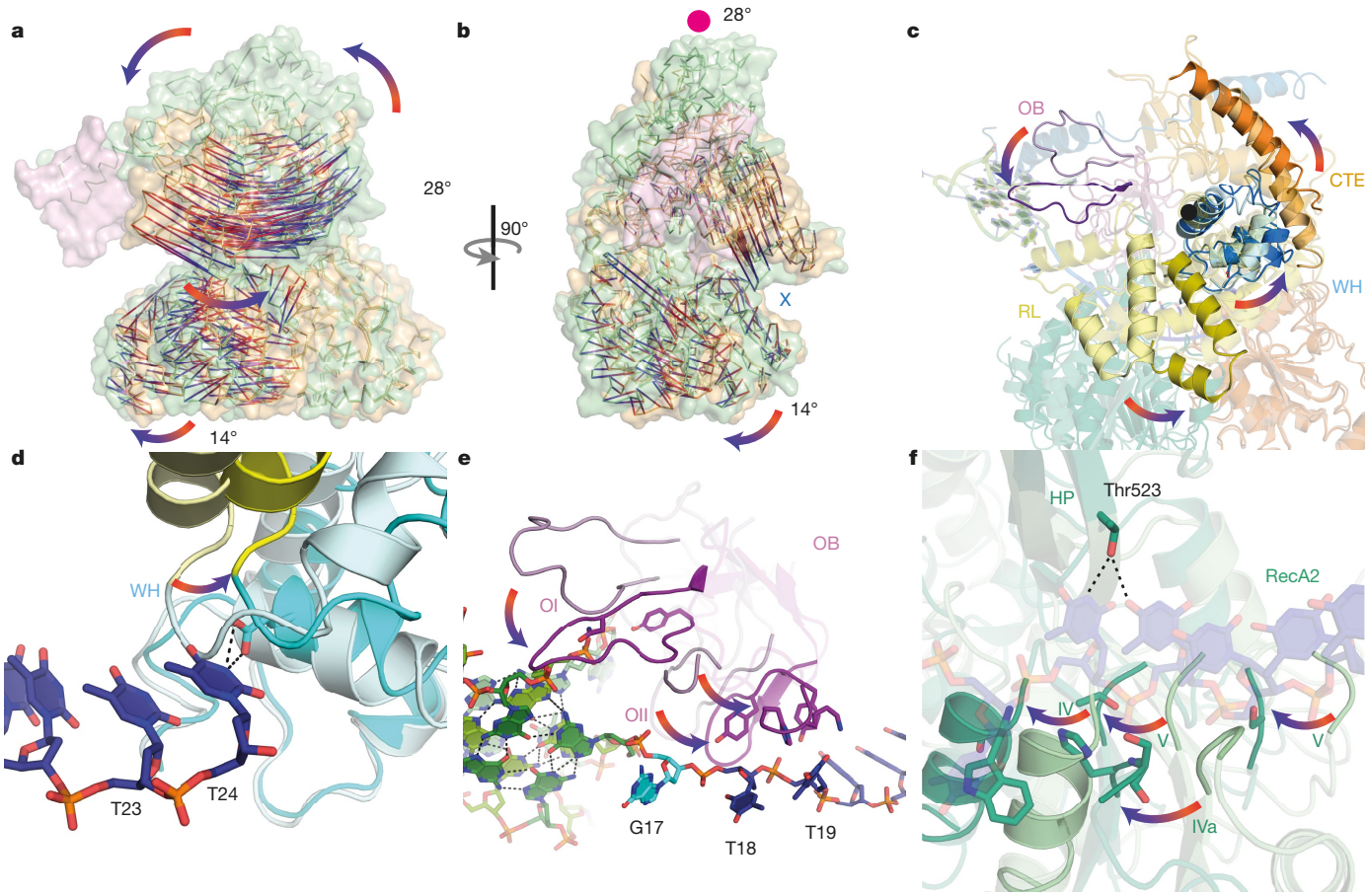

Fig. 3 | DNA-binding-induced structural transitions of DHX36. a, Superposition of DHX36-DSM–DNA^{Myc} and DHX36-core structures (green and orange, respectively; Cα vectors from red to blue) through RecA1. DNA^{Myc}, pink. **b**, As in **a**, rotated by 90°. Red circle and blue cross denote C-terminal domain rotation out of and into the plane, respectively. **c**, C-terminal sub-domains. Unliganded and DNA-bound, pastel and solid colours, respectively. Black circle, approximate axis of rotation. **d**, The WH in unliganded and DNA-bound states. T24 of DNA^{Myc} impinges on the loop linking WH and RL. **e**, The OI and OII loops of the OB domain in unliganded and DNA-bound states. **f**, The RecA2 domain in unliganded and DNA-bound states. Movement of conserved helicase motifs IV, IVa and V (Fig. 1a) is highlighted.

OB domain (OI loop) form extensive hydrogen bonds with the sugar-phosphate backbone of the 5′ leader (A1) and the G-quadruplex residues immediately following it (Fig. 2d). Formation of a composite G-quadruplex-binding surface between the DSM and OB domains explains why, in a previously reported NMR structure of a low-affinity complex between an 18-amino-acid DSM-derived peptide and a G-quadruplex[26], the DNA-binding-induced α-helix was out of register with that seen in our co-crystal structure (Extended Data Fig. 4c–g). In addition, DHX36 does not markedly discriminate between DNA and RNA substrates[4,27], and it recognizes the 3′ single-stranded region of DNA^{Myc} primarily by contacts with phosphates of its backbone (Fig. 2e, f). A second loop from OB (OII loop) contacts the backbones of T18 and T19 (Fig. 2e), while WH and the RecA1 domain interact with T23 and T24 (Fig. 2f).

Whereas other helicases can resolve both antiparallel and parallel G-quadruplexes[23], DHX36 has a strong preference for the latter, being inactive on fully antiparallel G-quadruplexes, and exhibiting reduced activity on G-quadruplexes with mixed parallel and antiparallel connectivity[21,22,26]. Bound to DHX36, DNA^{Myc} has three single-nucleotide double-chain-reversal loops (T5, T9, and G13) that do not sterically interfere with recognition of the top quartet by the DSM. Our structure suggests that the preference of DHX36 for parallel G-quadruplexes is likely to arise from the steric interference of diagonal and lateral loops with DSM binding. In addition, a 5′ G-tract with the opposite polarity would interfere with binding to the OI loop.

Our DHX36-DSM–DNA^{Myc} co-crystal structure provides an unprecedented view of the open, ATP-independent conformation adopted by a nucleic-acid bound DEAH/RHA helicase. Superposition of the RecA1 domains of our DHX36-core and DHX36-DSM–DNA^{Myc} structures shows that DNA binding alone induces rotations of the C-terminal and RecA2 domains by 28° and 14°, respectively (Fig. 3a–c). This conformation accommodates five stacked single-stranded (ss) DNA residues between the 5′ β-hairpin (HP) and the constriction formed by Arg297, Gln319 and Pro699 (Fig. 2e, f). Compared to the ATP analogue-bound and unliganded states, the nucleic-acid-interacting elements of RecA2 (motifs IV, IVa, and V; Fig. 1a) shift away from RecA1 by 6 Å—approximately the distance between successive nucleotides (Fig. 3f). HP acts as a fulcrum upon core opening, unstacking T18 and T19 on one side, and stabilizing the 3′ stack of nucleotides by hydrogen bonding with Thr523 on the other (Fig. 3e, f). The opening motion may allow the G-quadruplex to unfold by one residue, and is consistent with the one-nucleotide displacement of the DHX36-bound DNA^{Myc} structure relative to its free solution conformation (Extended Data Fig. 4a, b). Together with published structures of DEAH/RHA helicases in the ground[16,17], transition[15], and post-hydrolysis[13,14] states, our DHX36 structures support the hypothesis[17] that DEAH/RHA helicases cycle between four- and five-nucleotide stack states enforced by the HP and a 3′-constriction site to unwind their substrates (Extended Data Figs. 6, 7).

We examined structure-guided mutants of DHX36 using a single-molecule fluorescence resonance energy transfer (smFRET) assay previously developed to characterize the repetitive, ATP-independent G-quadruplex unfolding activity of the wild-type helicase[22] (Fig. 4a–c; Extended Data Fig. 2). The *Myc* promoter-derived parallel

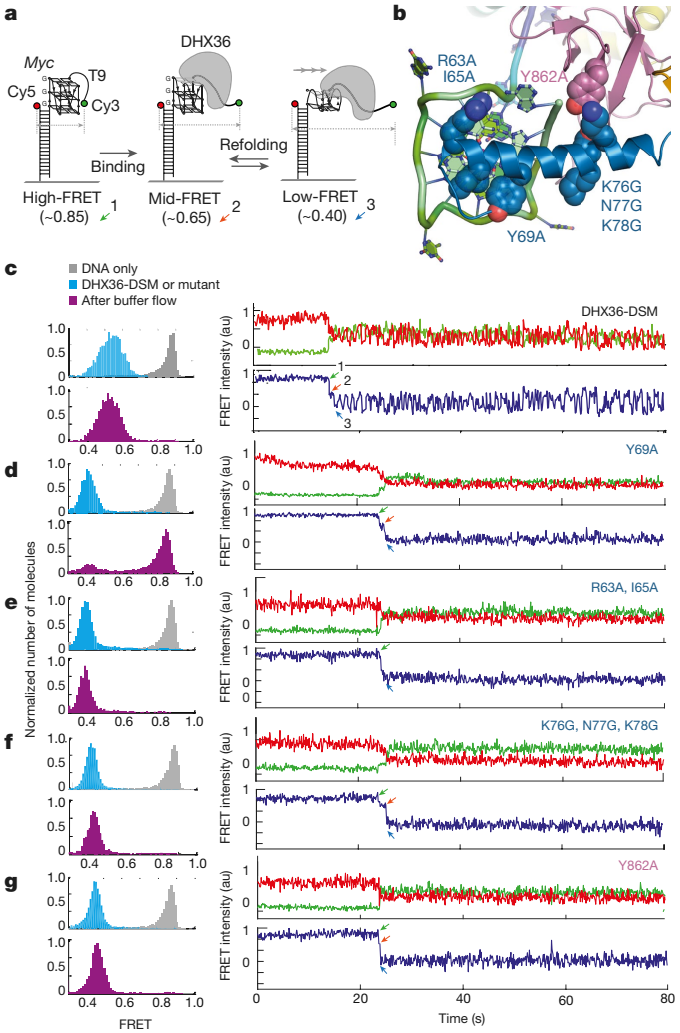

Fig. 4 | Single-molecule FRET analysis of DHX36-DSM mutants. **a**, Reporter with a G-quadruplex of the DNA^{Myc} sequence, and a nine-thimidine single-stranded 3′ tail. DHX36 shifts FRET from high (~0.8) to medium–low oscillation (~0.6, canonical DNA^{Myc}; ~0.4, reorganized DNA^{Myc}; Extended Data Figs. 2, 8). **b**, Structure-guided mutations. **c**, The DHX36-DSM crystallization construct remains DNA-bound upon flow and exhibits repetitive unfolding, similar to the wild type (Extended Data Fig. 2). **d**, The Y69A mutant lacks repetitive unfolding and dissociates from the G-quadruplex upon flow. **e–g**, Three mutants remain bound following flow, but lack repetitive unfolding. Each experiment was highly reproducible and in triplicate (data from more than 10,000 molecules per experiment).

G-quadruplex DNA that we use exhibits high FRET (Fig. 4a). Binding of DHX36 induces conformational changes, in which oscillations in FRET efficiency between medium and low (approximately 0.6 and 0.4, respectively) reflect repetitive unfolding between the canonical (with three complete G-quartets) and reorganized (pulled by one nucleotide) DNA^{Myc} G-quadruplex, respectively[28] (Extended Data Fig. 8). The repetitive unfolding activity is ATP-independent, as the absence of ATP or presence of non-hydrolysable ATP analogues do not affect it (Extended Data Fig. 2i, j). We hypothesize that the repetitive unfolding activity stems from ATP-independent helicase core opening and reciprocating rotation of the C-terminal domain. ATP is likely to be required only for release of DNA from the helicase, as rapid dissociation occurs upon ATP addition (Extended Data Fig. 2i, j).

Solution NMR of a DSM-derived peptide[26] (Extended Data Fig. 4c–g), as well as proteolytic susceptibility of the DHX36-DSM N terminus, indicate that α1 is intrinsically disordered[29], becoming fully α-helical upon interaction with the substrate G-quadruplex. Our mutagenesis shows that, as in other examples[29] of ligand-induced protein structure, binding free energy is distributed non-uniformly across the DSM. The R63A/I65A and KNK76GGG mutations of residues anchoring α1 on the G-quadruplex backbone are less deleterious than mutation of Tyr69 (Fig. 4b, d–g). Mutation of Tyr69, which stacks directly on the top quartet (Fig. 2a), weakens the helicase–DNA association to such an extent that, uniquely among the mutants examined, this protein dissociates from DNA upon buffer flow (Fig. 4d). Ligand-induced folding of α1 may allow DHX36 to mould to G-quadruplexes with different local structures, and even to antiparallel substrates with lower efficiency, during its mechanochemical cycle.

Our DHX36 co-crystal structure shows how a protein that evolved to recognize G-quadruplex-containing nucleic acids combines binding to the face and backbone of the G-quadruplex with recognition of both 5′ and 3′ single-stranded extensions. The unfolding activity of DHX36 was previously shown to be highly sensitive to the stability of its G-quadruplex substrates[5,22]. This sensitivity is consistent with our demonstration that nucleic acid binding energy is transduced by DHX36 into a discrete, directed pulling force arising from C-terminal domain rotation and helicase core opening. These ATP-independent structural changes remodel the G-quadruplex, resulting in a substrate unwound by a single nucleotide. Our analysis thus highlights the importance of ATP-independent structural changes for nucleic acid remodelling by a canonical DEAH/RHA helicase and constitutes a starting point for further structural analysis of the mechanochemical cycle of these important enzymes.

Online content

Any Methods, including any statements of data availability and Nature Research reporting summaries, along with any additional references and Source Data files, are available in the online version of the paper at https://doi.org/10.1038/s41586-018-0209-9.

Received: 23 September 2017; Accepted: 23 April 2018;
Published online 13 June 2018.

1. Hänsel-Hertsch, R., Di Antonio, M. & Balasubramanian, S. DNA G-quadruplexes in the human genome: detection, functions and therapeutic potential. *Nat. Rev. Mol. Cell Biol.* **18**, 279–284 (2017).
2. Rhodes, D. & Lipps, H. J. G-quadruplexes and their regulatory roles in biology. *Nucleic Acids Res.* **43**, 8627–8637 (2015).
3. Mendoza, O., Bourdoncle, A., Boulé, J. B., Brosh, R. M. J. Jr & Mergny, J. L. G-quadruplexes and helicases. *Nucleic Acids Res.* **44**, 1989–2006 (2016).
4. Giri, B. et al. G4 resolvase 1 tightly binds and unwinds unimolecular G4-DNA. *Nucleic Acids Res.* **39**, 7161–7178 (2011).
5. Chen, M. C., Murat, P., Abecassis, K., Ferré-D'Amaré, A. R. & Balasubramanian, S. Insights into the mechanism of a G-quadruplex-unwinding DEAH-box helicase. *Nucleic Acids Res.* **43**, 2223–2231 (2015).
6. Vaughn, J. P. et al. The DEXH protein product of the DHX36 gene is the major source of tetramolecular quadruplex G4-DNA resolving activity in HeLa cell lysates. *J. Biol. Chem.* **280**, 38117–38120 (2005).
7. Lattmann, S., Stadler, M. B., Vaughn, J. P., Akman, S. A. & Nagamine, Y. The DEAH-box RNA helicase RHAU binds an intramolecular RNA G-quadruplex in TERC and associates with telomerase holoenzyme. *Nucleic Acids Res.* **39**, 9390–9404 (2011).
8. McRae, E. K. S. et al. Human DDX21 binds and unwinds RNA guanine quadruplexes. *Nucleic Acids Res.* **45**, 6656–6668 (2017).
9. Nie, J. et al. Post-transcriptional regulation of Nkx2–5 by RHAU in heart development. *Cell Reports* **13**, 723–732 (2015).
10. Lai, J. C. et al. The DEAH-box helicase RHAU is an essential gene and critical for mouse hematopoiesis. *Blood* **119**, 4291–4300 (2012).
11. Sexton, A. N. & Collins, K. The 5′ guanosine tracts of human telomerase RNA are recognized by the G-quadruplex binding domain of the RNA helicase DHX36 and function to increase RNA accumulation. *Mol. Cell. Biol.* **31**, 736–743 (2011).
12. Booy, E. P. et al. The RNA helicase RHAU (DHX36) unwinds a G4-quadruplex in human telomerase RNA and promotes the formation of the P1 helix template boundary. *Nucleic Acids Res.* **40**, 4110–4124 (2012).
13. Walbott, H. et al. Prp43p contains a processive helicase structural architecture with a specific regulatory domain. *EMBO J.* **29**, 2194–2204 (2010).
14. He, Y., Andersen, G. R. & Nielsen, K. H. Structural basis for the function of DEAH helicases. *EMBO Rep.* **11**, 180–186 (2010).
15. Prabu, J. R. et al. Structure of the RNA helicase MLE reveals the molecular mechanisms for uridine specificity and RNA-ATP coupling. *Mol. Cell* **60**, 487–499 (2015).
16. Tauchert, M. J., Fourmann, J. B., Lührmann, R. & Ficner, R. Structural insights into the mechanism of the DEAH-box RNA helicase Prp43. *eLife* **6**, 762 (2017).

17. He, Y., Staley, J. P., Andersen, G. R. & Nielsen, K. H. Structure of the DEAH/RHA ATPase Prp43p bound to RNA implicates a pair of hairpins and motif Va in translocation along RNA. *RNA* **23**, 1110–1124 (2017).
18. Chen, M. C. & Ferré-D'Amaré, A. R. Structural basis of DEAH/RHA helicase activity. *Crystals* **7**, 253 (2017).
19. Lattmann, S., Giri, B., Vaughn, J. P., Akman, S. A. & Nagamine, Y. Role of the amino terminal RHAU-specific motif in the recognition and resolution of guanine quadruplex-RNA by the DEAH-box RNA helicase RHAU. *Nucleic Acids Res.* **38**, 6219–6233 (2010).
20. Ambrus, A., Chen, D., Dai, J., Jones, R. A. & Yang, D. Solution structure of the biologically relevant G-quadruplex element in the human c-MYC promoter. Implications for G-quadruplex stabilization. *Biochemistry* **44**, 2048–2058 (2005).
21. Smaldino, P. J. et al. Mutational dissection of telomeric DNA binding requirements of G4 resolvase 1 shows that G4-structure and certain 3′-tail sequences are sufficient for tight and complete binding. *PLoS One* **10**, e0132668 (2015).
22. Tippana, R., Hwang, H., Opresko, P. L., Bohr, V. A. & Myong, S. Single-molecule imaging reveals a common mechanism shared by G-quadruplex-resolving helicases. *Proc. Natl Acad. Sci. USA* **113**, 8448–8453 (2016).
23. Yangyuoru, P. M., Bradburn, D. A., Liu, Z., Xiao, T. S. & Russell, R. The G-quadruplex (G4) resolvase DHX36 efficiently and specifically disrupts DNA G4s via a translocation-based helicase mechanism. *J. Biol. Chem.* **293**, 1924–1932 (2018).
24. Phan, A. T., Modi, Y. S. & Patel, D. J. Propeller-type parallel-stranded G-quadruplexes in the human *c-myc* promoter. *J. Am. Chem. Soc.* **126**, 8710–8716 (2004).
25. Ohnmacht, S. A. & Neidle, S. Small-molecule quadruplex-targeted drug discovery. *Bioorg. Med. Chem. Lett.* **24**, 2602–2612 (2014).
26. Heddi, B., Cheong, V. V., Martadinata, H. & Phan, A. T. Insights into G-quadruplex specific recognition by the DEAH-box helicase RHAU: Solution structure of a peptide-quadruplex complex. *Proc. Natl Acad. Sci. USA* **112**, 9608–9613 (2015).
27. Creacy, S. D. et al. G4 resolvase 1 binds both DNA and RNA tetramolecular quadruplex with high affinity and is the major source of tetramolecular quadruplex G4-DNA and G4-RNA resolving activity in HeLa cell lysates. *J. Biol. Chem.* **283**, 34626–34634 (2008).
28. Tippana, R., Xiao, W. & Myong, S. G-quadruplex conformation and dynamics are determined by loop length and sequence. *Nucleic Acids Res.* **42**, 8106–8114 (2014).
29. Wright, P. E. & Dyson, H. J. Intrinsically disordered proteins in cellular signalling and regulation. *Nat. Rev. Mol. Cell Biol.* **16**, 18–29 (2015).

Acknowledgements We thank the staff of sector 5 of ALS and beamline 17-ID-B of APS for crystallographic data collection; Y. He, National Heart, Lung and Blood Institute (NHLBI) for protein production; G. Piszczek (NHLBI) for DSC; R. Levine and D.-Y. Lee (NHLBI) for mass spectrometry; and C. Fagan, C. Jones, T. Numata, R. Trachman III, K. Warner, and J. Zhang for discussions. This work was partly conducted at the ALS on the Berkeley Center for Structural Biology beamlines, which are supported by the US National Insitutes of Health (NIH). Use of ALS and APS was supported by the US Department of Energy. This work was supported in part by the NIH (GM105453, S.M.), American Chemical Society (RSG-12-066-01-DMC, S.M.), National Science Foundation Physics Frontiers Center Program (0822613, S.M.), Wellcome Trust (099232/z/12/z, S.B.), European Research Council (339778, S.B.), Cancer Research UK (C12303/A17197 and C9681/A18618, S.B.), NIH-Oxford-Cambridge Scholars Program (M.C.C.), Cambridge Trust (M.C.C.), and the intramural program of the NHLBI, NIH.

Reviewer information *Nature* thanks D. Patel, K. Raney and V. Zakian for their contribution to the peer review of this work.

Author contributions M.C.C., P.M., S.B., and A.R.F.-D. conceived the project; M.C.C. performed protein expression, crystallization and structure determination; N.A.D. prepared mutants and characterized model G-quadruplexes; R.T. and S.M. performed smFRET; and M.C.C. and A.R.F.-D. wrote the manuscript.

Competing interests The authors declare no competing interests.

Additional information
Extended data is available for this paper at https://doi.org/10.1038/s41586-018-0209-9.
Supplementary information is available for this paper at https://doi.org/10.1038/s41586-018-0209-9.
Reprints and permissions information is available at http://www.nature.com/reprints.
Correspondence and requests for materials should be addressed to A.R.F.-D.
Publisher's note: Springer Nature remains neutral with regard to jurisdictional claims in published maps and institutional affiliations.

METHODS

Protein expression and purification. *Bos taurus* DHX36-core, DHX36-core-SeMet, and DHX36-DSM were expressed in *Escherichia coli* LOBSTR (DE3)[30]. All proteins have C-terminal 8His tags and DHX36-DSM also has an N-terminal GST tag. Starter cultures were grown at 37 °C in MDAG-135 medium[31]. Production cultures in Terrific broth were induced with 1 mM IPTG at 20 °C and grown overnight. Lysis was in 50 mM HEPES-KOH (pH 7.5), 0.5 M KCl, 10 mM β-mercaptoethanol, 0.1% (v/v) Tween-20, 10% (v/v) glycerol, and Sigmafast EDTA-free protease inhibitor cocktail. Lysate supernatant was treated with polyethyleneimine (0.05%, v/v) and loaded on a Ni-NTA Superflow (Qiagen) column. The proteins were eluted with 500 mM imidazole. DHX36-core was further purified on a Superdex 200 PG column (GE Healthcare) in 20 mM HEPES-KOH pH 7.5, 150 mM KCl, 10% (v/v) glycerol, 0.5 mM TCEP, and 2.5 mM $MgCl_2$. For DHX36-DSM, the eluate from the Ni-NTA column was loaded onto GSTrap 4B (GE Healthcare) column, washed with 20 mM HEPES-KOH (pH 7.5), 150 mM KCl, 10% (v/v) glycerol, and 1 mM TCEP (pH 7.0), and eluted with 25 mM reduced glutathione. The eluted DHX36-DSM was incubated at 20 °C with TEV protease (1:10 mass ratio) for 1 h. Then, DNA^{Myc} (5′-AGG GTG GGT AGG GTG GGT TTT TTT-3′) was added (2:1 DHX36-DSM:DNA^{Myc} molar ratio) and the mixture was incubated for 30 min at 21 °C. The mixture was dialysed (50 kDa MWCO membrane) against 50 mM HEPES-KOH (pH 7.5), 150 mM KCl, and 10% (v/v) glycerol overnight at 4 °C and then incubated with Amintra GST resin (Expedeon) for 1 h at 4 °C. For crystallization, the complex was reductively methylated as described[32]. Electrospray ionization mass spectrometry (ESI-MS) indicated a mass of 109,098 ± 2 Da, which corresponds to the dimethylation of 63 out of a total of 66 lysines in DHX36-DSM. After methylation, the DHX36-DSM–DNA^{Myc} complex was further purified by size-exclusion chromatography as DHX36-core. For expression of DHX36-core-SeMet, PASM-5052 autoinduction expression medium[31] was inoculated with a starter culture grown in MDAG-135 medium. Cultures were grown at 20 °C for ~6 days. Purification was as described above. The mass of DHX36-core-Semet by ESI-MS was 101,011 ± 2 Da, corresponding to a methionine labelling efficiency of 95.8%. All proteins were purified to >98% homogeneity, with the exception of DHX36-core-SeMet, which was purified to >80% homogeneity (as judged by Coomassie blue staining of serial dilutions analysed by SDS–PAGE). All DHX36 constructs used in this study contain a deletion of residues 1–54, which encompasses the Gly-rich region. DHX36-core contains a deletion of residues 1–149. DHX36-AAA contains a KKK192AAA mutation to prevent spontaneous proteolysis. DHX36-DSM contains a deletion of residues 111–159 and surface entropy reduction mutations EEK435YYY and KDTK752AATA. All mutations used to generate the various constructs (DHX36-core, DHX36-AAA, DHX36-DSM, and structure-guided mutants) were generated using the QuikChange Lighting kit (Agilent). DHX36-DSM mutants for smFRET were purified essentially as above, but after elution from the GSTrap 4B column, the GST tag was cleaved by TEV protease in buffer with 400 mM KCl and removed by a second passage through the GSTrap 4B resin. The mutant proteins were then dialysed against 50 mM HEPES-KOH (pH 7.5), 600 mM KCl, 10% (v/v) glycerol and 1 mM TCEP (pH 7.0) overnight at 4 °C and purified by size-exclusion chromatography (Superdex 200 PG, GE Healthcare) in the same buffer.

Crystallization and diffraction data collection. Hanging drops were prepared by mixing 1 μl each of DHX36-core (5 g/l) and reservoir (0.2 M ammonium citrate (pH 7.0) and 20% (w/v) PEG3350), and were equilibrated by vapour diffusion at 21 °C. DHX36-core-AlF_4^- was crystallized under the same conditions in the presence of ADP•AlF_4^- (1 mM). ADP•AlF_4^- was prepared by mixing in order the following molar ratio: 1 part Na-ADP (100 mM), 1 part $AlCl_3$ (1 M), and 5 parts NaF (500 mM). DHX36-Core-BeF_3^- was crystallized by vapour diffusion at 21 °C using a reservoir consisting of 0.2 M potassium sodium tartrate (pH 7.4) and 20% (w/v) PEG 3350. ADP•BeF_3^- was prepared using the same protocol as above, except replacing $AlCl_3$ with $BeSO_4$. DHX36-Core-SeMet crystals were grown by vapour diffusion at 21 °C by combining 1.5 μl protein solution (5 g/l), 1 μl reservoir (50 mM sodium cacodylate (pH 7.1), 150 mM ammonium carbonate (pH 6.9), and 13.8% (v/v) 2-propanol), and 0.5 μl microseed stock. The stock was made by crushing crystals of DHX36-core. All DHX36-core crystals were soaked in their respective reservoir solutions supplemented with 30% (v/v) glycerol before flash-freezing in liquid nitrogen. All DHX36-core crystals grew as rhombohedra to maximum dimensions of 500 × 300 × 300 μm^3 in 1–2 weeks. DHX36-DSM complexed with DNA^{Myc} was crystallized at 21 °C by hanging-drop vapour diffusion. Drops were prepared by combining complex solution (1.5 μl, 3 g/l), reservoir (1.0 μl) and microseed stock (0.5 μl). The reservoir consisted of 200 mM sodium malonate (pH 7.0) and 25% (w/v) PEG 3350. The seed stock was from crystals of unmethylated DHX36-DSM in complex with DNA^{Myc} (grown in 45 mM MES-monohydrate (pH 5.7), 180 mM KCl, 29 mM $MgCl_2$, 4.5% (w/v) PEG 8000, 10 mM HEPES-NaOH (pH 7.5), and 3% (v/v) 2-propanol). Methylated DHX36-DSM–DNA^{Myc} crystals grew as plates to maximum dimensions of 500 × 100 × 5 μm^3 in 2–8 weeks. After growth, the reservoir solution was changed successively to 30% and 40% (w/v) PEG 3350 (other components unchanged) for a week each. Crystals, mounted on 90° bent loops (Mitegen), were flash-frozen in liquid nitrogen without further cryoprotection. Diffraction data were collected at 100 K in rotation mode with 0.9792 Å X-radiation at beamlines 5.0.1 and 5.0.2 of the Advanced Light Source (ALS), Lawrence Berkeley National Laboratory, and beamline 17-ID-B of the Advanced Photon Source (APS), Argonne National Laboratory. Data were indexed, integrated, and scaled using HKL2000[33] (Extended Data Tables 1, 2).

Structure determination and refinement. Data sets from five DHX36-core-SeMet crystals were scaled and merged together in HKL2000 (Extended Data Table 2). A heavy-atom substructure comprised of 18 selenium atoms was identified in this high-redundancy data set by HySS[34] implemented in PHENIX AutoSol[35]. The resulting experimental SAD phases (mean overall figure of merit = 0.56) were density-modified with RESOLVE[36] to produce an electron density map in which manual model building using COOT[37] could begin (Extended Data Fig. 3). Iterative rounds of manual model building interspersed with rigid-body, simulated annealing, energy minimization, and individual isotropic *B*-factor refinement in PHENIX produced a near-complete model (R_{free} = 35.2) that could be placed (TFZ = 20.2) into the DHX36-core data set using PHASER[38]. Further rounds of manual model building interspersed with refinement produced the current DHX36-core, DHX36-core-AlF_4^-, and DHX36-core-BeF_3^- models (Extended Data Table 1). Refined coordinates of the RecA1 domain from the 2.2 Å-resolution DHX36-core structure were used as a search model against the DHX36-DSM–DNA^{Myc} data set, yielding[38] a solution with TFZ = 13.1. Subsequently, the RecA2 and C-terminal domains were successively placed (TFZs = 25.1 and 22.4, respectively). Rigid-body refinement followed by simulated annealing and restrained individual isotropic *B*-factor refinement was in turn followed by manual model building and further refinement to yield the current model of the DNA–protein complex (Extended Data Table 1). Coordinate precision estimates are from PHENIX. Structure figures were prepared with PyMol and Chimera[39,40].

Differential scanning calorimetry. Three DNA^{Myc} sequences (IDT, Extended Data Fig. 5a) at 0.1 mM concentration in 20 mM cacodylic acid-KOH (pH 7.2) and either 20 mM or 150 mM KCl were heated at 95 °C for 2.5 min, placed on ice for 10 min, and warmed to 21 °C over 20 min. The DNAs were analysed by size-exclusion chromatography (Superdex 75 Increase, GE Healthcare) in 20 mM cacodylic acid-KOH (pH 7.2) and 150 mM KCl (Extended Data Fig. 5b). For DSC, DNA samples prepared in 20 mM cacodylic acid-KOH (pH 7.2) and 20 mM KCl were degassed for 5-7 min before measurements (MicroCal VP-DSC differential scanning calorimeter). Thermograms were acquired between 20-105 °C at a scan rate of 0.5 °C min^{-1} and at a constant pressure of 24 p.s.i. Three to five heating and cooling cycles were collected at least in duplicate for two independent preparations of each DNA sequence. Thermograms were highly reproducible (Extended Data Fig. 5c), and were analysed with Origin software (OriginLab). The reference 'buffer versus buffer' (20 mM cacodylic acid-KOH (pH 7.2) and 20 mM KCl) was subtracted from the sample data before curve-fitting (Levenberg-Marquardt nonlinear least-squares method) to determine T_m and ΔH.

Single-molecule FRET analyses. smFRET analyses of DHX36-DSM and site-directed mutants were performed as described[22,28].

Reporting summary. Further information on experimental design is available in the Nature Research Reporting Summary linked to this paper.

Data availability. Atomic coordinates and structure factors have been deposited in the RCSB Protein Data Bank (PDB) with accession numbers 5VHE for DHX36-DSM–DNA^{Myc}, 5VHA for DHX36-core, 5VHC for DHX36-core-BeF_3^-, and 5VHD for DHX36-core-AlF_4^-.

30. Andersen, K. R., Leksa, N. C. & Schwartz, T. U. Optimized *E. coli* expression strain LOBSTR eliminates common contaminants from His-tag purification. *Proteins* **81**, 1857–1861 (2013).
31. Studier, F. W. Protein production by auto-induction in high density shaking cultures. *Protein Expr. Purif.* **41**, 207–234 (2005).
32. Rayment, I. et al. Three-dimensional structure of myosin subfragment-1: a molecular motor. *Science* **261**, 50–58 (1993).
33. Otwinowski, Z. & Minor, W. Processing of diffraction data collected in oscillation mode. *Methods Enzymol.* **276**, 307–326 (1997).
34. Grosse-Kunstleve, R. W. & Adams, P. D. Substructure search procedures for macromolecular structures. *Acta Crystallogr. D Biol. Crystallogr.* **59**, 1966–1973 (2003).
35. Adams, P. D. et al. PHENIX: a comprehensive Python-based system for macromolecular structure solution. *Acta Crystallogr. D Biol. Crystallogr.* **66**, 213–221 (2010).
36. Terwilliger, T. C. Maximum-likelihood density modification. *Acta Crystallogr. D Biol. Crystallogr.* **56**, 965–972 (2000).
37. Emsley, P. & Cowtan, K. Coot: model-building tools for molecular graphics. *Acta Crystallogr. D Biol. Crystallogr.* **60**, 2126–2132 (2004).
38. McCoy, A. J. et al. Phaser crystallographic software. *J. Appl. Crystallogr.* **40**, 658–674 (2007).
39. DeLano, W. L. *The PyMOL Molecular Graphics System* (DeLano Scientific, 2002).

40. Pettersen, E. F. et al. UCSF Chimera—a visualization system for exploratory research and analysis. *J. Comput. Chem.* **25**, 1605–1612 (2004).
41. Tauchert, M. J., Fourmann, J.-B., Christian, H., Lührmann, R. & Ficner, R. Structural and functional analysis of the RNA helicase Prp43 from the thermophilic eukaryote *Chaetomium thermophilum*. *Acta Crystallogr. F* **72**, 112–120 (2016).
42. Chalupníková, K. et al. Recruitment of the RNA helicase RHAU to stress granules via a unique RNA-binding domain. *J. Biol. Chem.* **283**, 35186–35198 (2008).
43. Sievers, F. et al. Fast, scalable generation of high-quality protein multiple sequence alignments using Clustal Omega. *Mol. Syst. Biol.* **7**, 539 (2011).

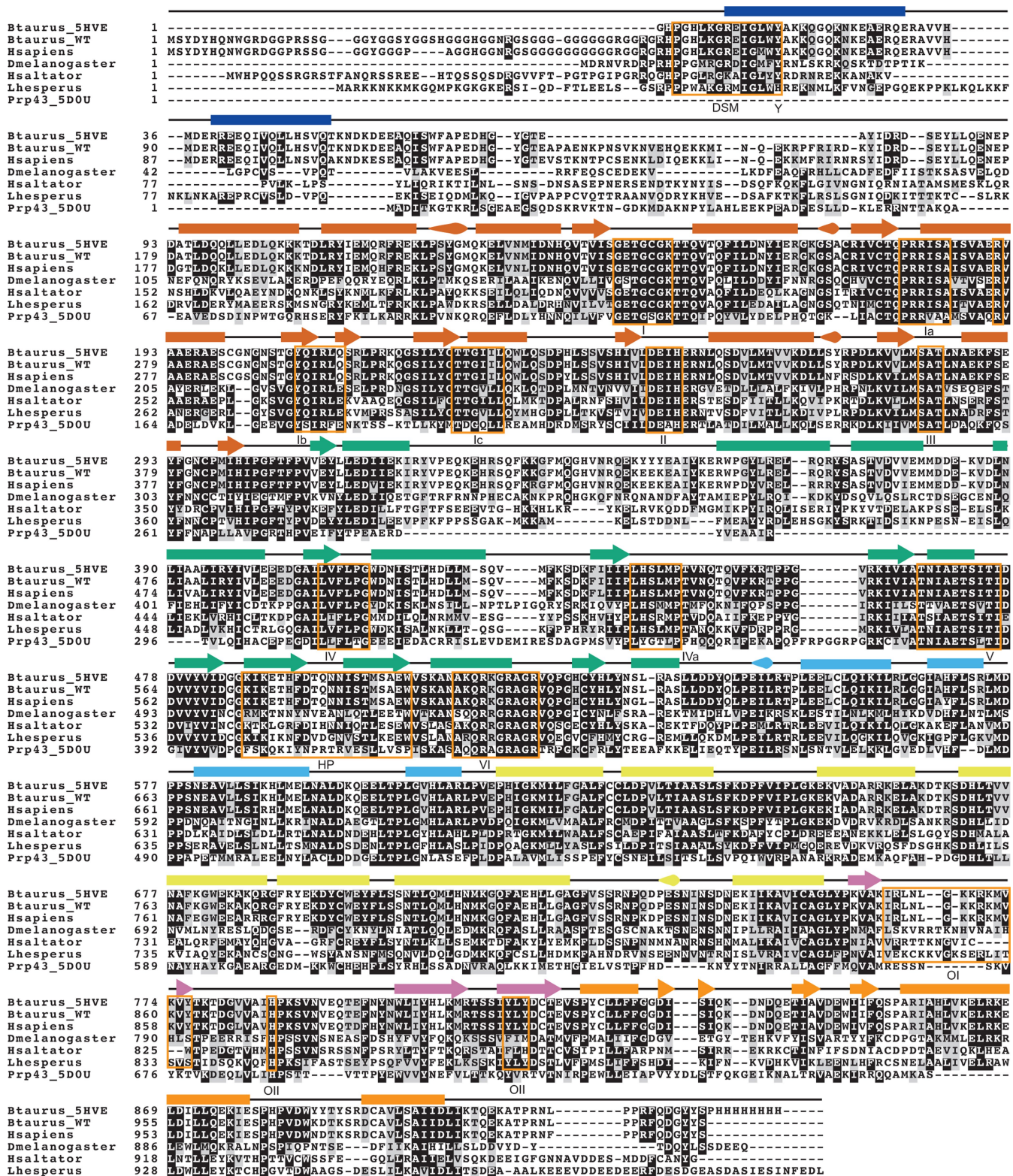

Extended Data Fig. 1 | Sequence alignment of DHX36 orthologues. The *Bos taurus* DHX36 construct used to solve the DHX36-DSM–DNA^{Myc} co-crystal structure (PDB ID: 5VHE), wild-type *Bos taurus* DHX36, *Homo sapiens* DHX36, *Drosophila melanogaster* DHX36, *Herpegnathos saltator* DHX36, *Latrodectus hesperus* DHX36, and the *Chaetomium thermophilum* Prp43 crystallization construct[41] (PDB ID: 5D0U) are aligned with a 0.5 threshold for similarity (grey shading). The glycine-rich region is responsible for DHX36 recruitment to stress granules[42], but it is not necessary for DHX36 binding or resolution of G-quadruplexes. Identical residues are shaded in black. Secondary structure from the DHX36-DSM–DNA^{Myc} co-crystal structure is indicated above each alignment section, with arrow, rectangle and cone denoting α-helix, β-strand, and 3_{10}-helix, respectively. Secondary structure is colour-coded by domain or subdomain as in Fig. 1. Alignment was performed with Clustal Omega[43] and depicted using BoxShade (http://sourceforge.net/projects/boxshade/).

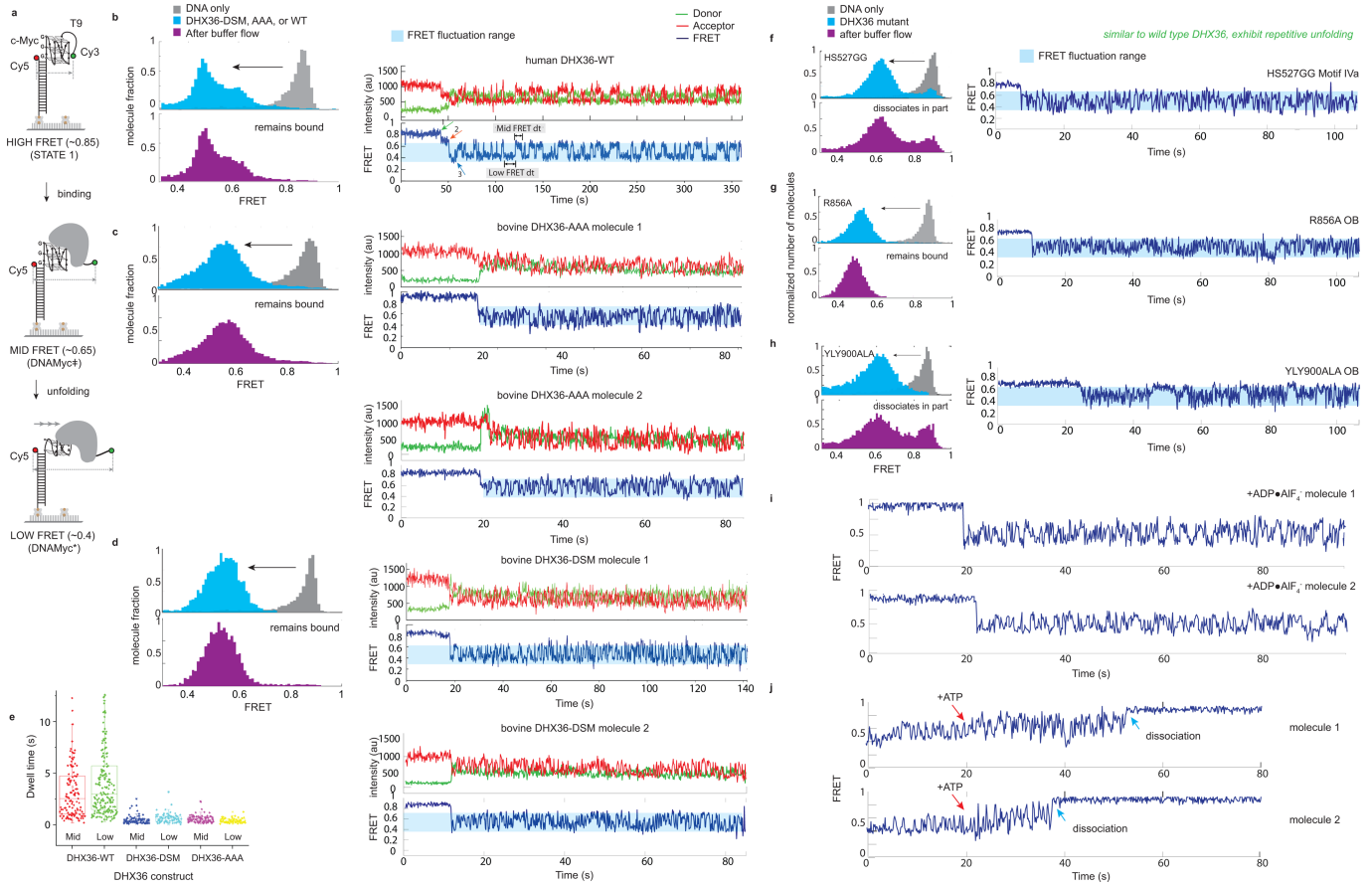

Extended Data Fig. 2 | Single-molecule FRET analysis of wild-type human DHX36 and bovine DHX36 constructs. a, Schematic of the smFRET assay[22,28]. See Extended Data Fig. 8 for FRET state assignments. **b**, Binding of wild-type human DHX36 (DHX36-WT)[22] to the G-quadruplex substrate, induces a shift from a high to medium and low FRET states (grey and cyan histograms, respectively). The shift is interpreted as the binding of DHX36 to the G-quadruplex substrate. Upon buffer flow, dissociation is not observed (purple histogram). Wild-type human DHX36 displays repetitive unfolding activity[22], as indicated by the oscillation between medium and low FRET states after binding to the G-quadruplex substrate (blue trace). **c**, Binding of wild-type bovine DHX36 (incorporating a KKK192AAA mutation to prevent spontaneous proteolysis; DHX36-AAA) to the G-quadruplex substrate induces a shift from a high FRET state to medium and low FRET states (grey and cyan histograms, respectively). The shift is interpreted as the binding of DHX36 to the G-quadruplex substrate. Upon buffer flow, dissociation is not observed (purple histogram). Wild-type bovine DHX36 (DHX36-AAA) displays repetitive unfolding activity, as indicated by the oscillation between low and medium FRET states after binding to the G-quadruplex substrate (blue trace). FRET traces are shown for two molecules. **d**, Deletion of residues 111–159, mutation EEK435YYY, and mutation KDTK752AATA to generate DHX36-DSM does not impair G-quadruplex binding or repetitive unfolding activity. FRET traces are shown for two molecules. **e**, Dwell time comparison between human DHX36-WT (grey bars), bovine wild-type DHX36 (DHX36-AAA, cyan bars) and bovine DHX36-DSM (orange bars). All three proteins show a comparable FRET range, and the two bovine constructs exhibit similar dwell times between the medium and low FRET states. Dwell times between the bovine constructs and the human construct are different, probably owing to interspecies differences. Each experiment was performed three times. Data are reported as box dot plots, with the data centre as the median ± s.e. of 1,000 dwell times from 200 representative molecules. **f**–**h**, Mutation of motif IVa (hook loop) (**f**), the OB subdomain residue R856 (**g**), and OII does not result in impaired repetitive unfolding activity (**h**). However, partial dissociation following washing is observed with the motif IVa (**f**) and OII mutation (**h**). **i**, Pre-incubation of bovine DHX36-AAA with the non-hydrolysable ATP γ-phosphate hydrolysis transition state mimic ADP•AlF_4^- does not affect repetitive unfolding activity on G-quadruplex substrates. **j**, Addition of ATP (red arrow) while DHX36-AAA is displaying repetitive unfolding activity on G-quadruplex substrates results in DHX36 dissociation (blue arrow) on the seconds timescale. Each experiment was repeated three times with highly similar results. Each measurement yields data from at least 10,000 molecules.

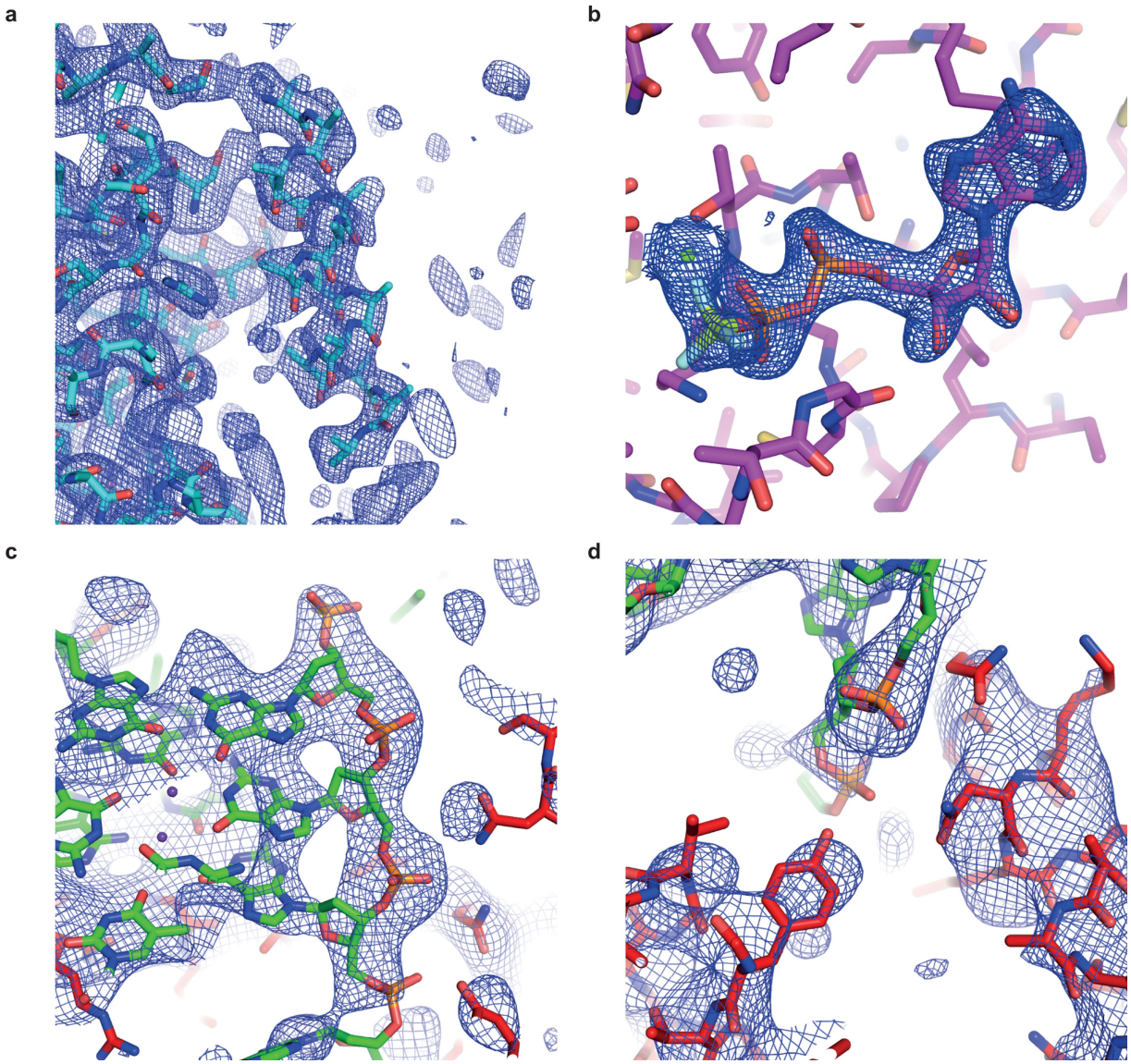

Extended Data Fig. 3 | Electron density maps superimposed on refined structures. a, Portion of the density-modified 3.1 Å resolution experimental SAD electron density map of selenomethionyl DHX36-core contoured at 1 s.d. above mean peak height, superimposed on a partially refined atomic model (see Methods). **b**, Portion of the 2.5 Å resolution simulated-annealing omit $2|F_o|-|F_c|$ electron density map of DHX36-core in complex with ADP•BeF_3^- (PDB ID: 5VHC) contoured at 1.5. **c**, Portion of a simulated annealing-omit $2|F_o|-|F_c|$ electron density map of the DHX36-DSM–DNA^{Myc} complex corresponding to the G-quadruplex, contoured at 1 s.d. **d**, Portion of the electron density map (**c**) corresponding to the OI loop and the DSM helix (lower left and right, respectively). A portion of the DNA is in the upper centre.

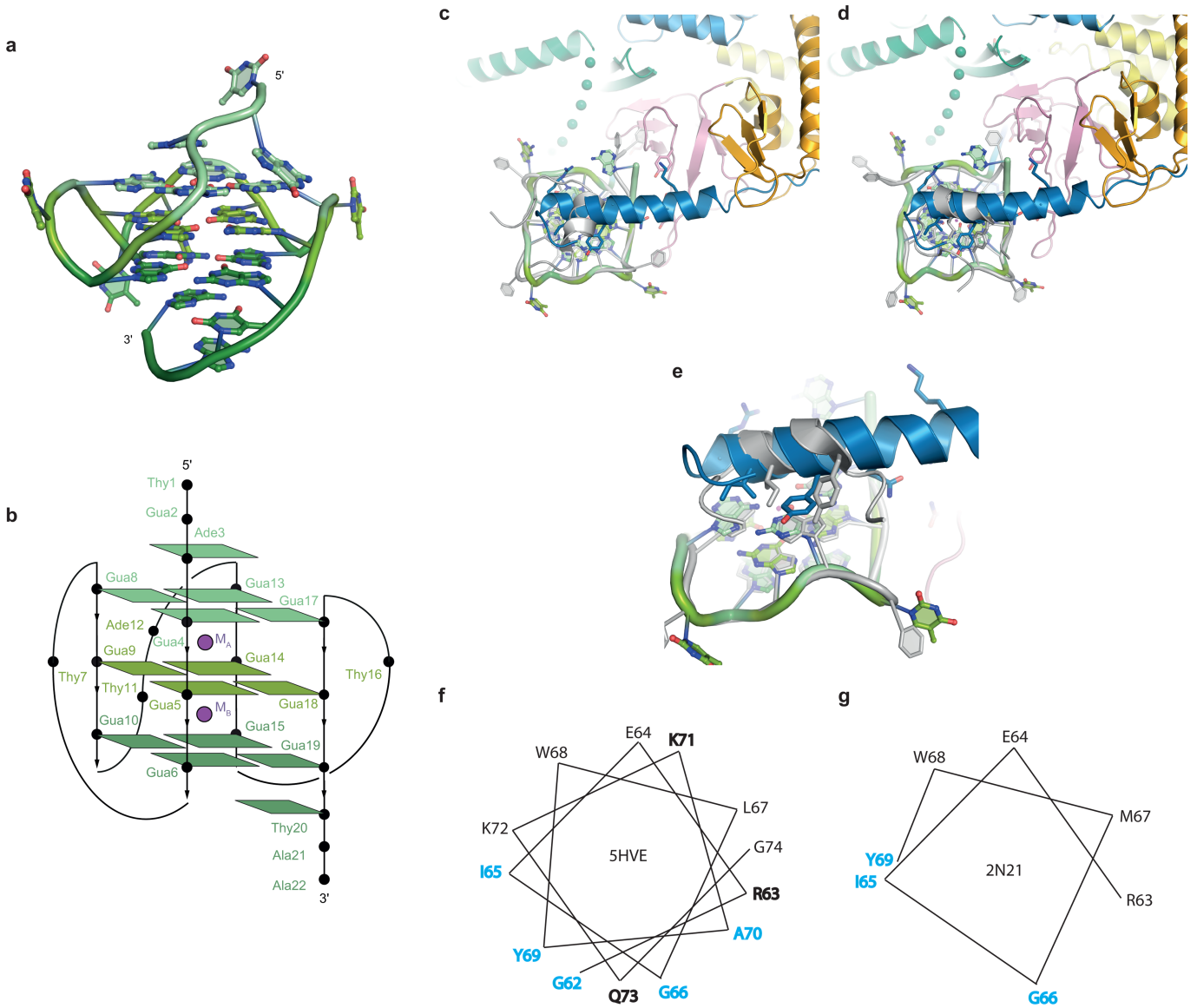

Extended Data Fig. 4 | Comparison of DNA^{Myc} and DSM with solution structures of a *c-Myc* promoter sequence-derived parallel DNA G-quadruplex and DSM bound to a parallel DNA G-quadruplex. **a**, Cartoon representation of the *Myc* G-quadruplex structure[20,24] adopted by the DNA of sequence 5′-TGA GGG (T) GGG TA GGG (T) GGG TAA-3′ (PDB ID: 1XAV). Underlined nucleotides form the three G-quartets. **b**, Schematic of the *Myc* G-quadruplex (PDB ID: 1XAV); compare with Fig. 2a. The DHX36-DSM–DNA^{Myc} co-crystal structure (PDB ID 5VHE; coloured as in Fig. 1) was superimposed through the G-quadruplex with the solution structure[26] (PDB ID: 2N21; grey) of a DSM-derived peptide bound to a G-quadruplex. **c**, If the superposition is performed so that the 5′ and 3′ G-tracts of the G-quadruplexes from the two structures align, the α-helix of the solution structure of the DSM-derived peptide is oriented approximately 90° with respect to the DSM α-helix from the DHX36-DSM–DNA^{Myc} co-crystal structure. **d**, If arbitrarily rotated along the quadruplex four-fold axis, the DSM α-helices from both structures approximately align. **e**, Even with this rotation, the two structures differ in the DSM side chains presented to the DNA. **f**, **g**, Helical wheel representations of the DSM α-helices from the DHX36-DSM–DNA^{Myc} co-crystal structure and the solution structure of the DSM-derived peptide bound to a G-quadruplex, respectively. Residues in cyan and bold make van der Waals contacts with the G-quadruplex face and hydrogen bond with the DNA backbone, respectively. Residue numbers correspond to the DHX36-DSM–DNA^{Myc} co-crystal structure.

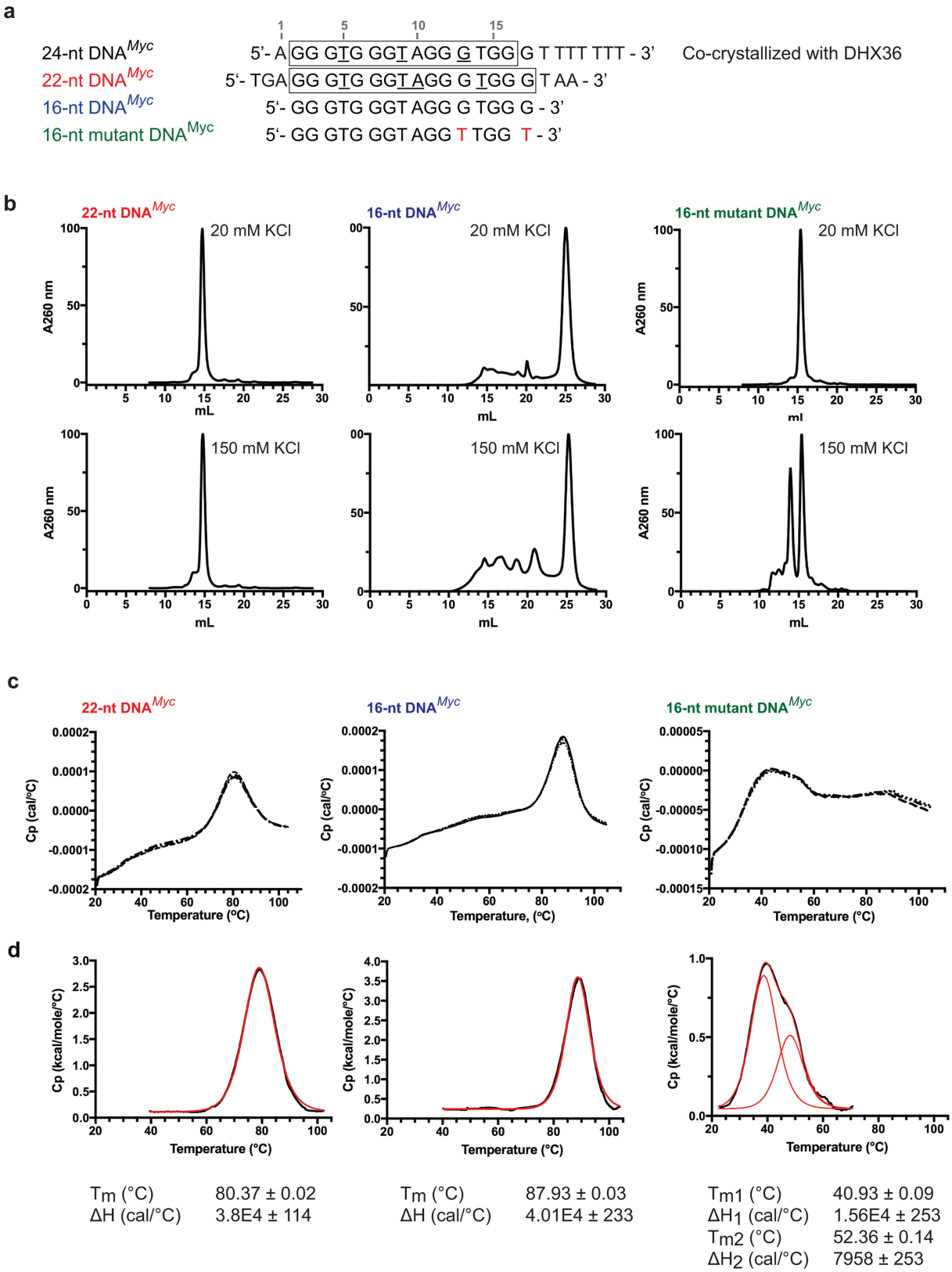

Extended Data Fig. 5 | See next page for caption.

Extended Data Fig. 5 | Analysis of DNA^{Myc} conformers by differential scanning calorimetry (DSC). a, DNA constructs used in the analysis. DNA^{Myc}, DNA used for co-crystallization with DHX36-DSM (see Methods). Residues that form a three-tiered G-quadruplex in the complex and those that form propeller loops are boxed and underlined, respectively. 22-nt DNA^{Myc}, DNA used for solution NMR analysis[20]. Residues that form a three-tiered G-quadruplex and those that form propeller loops in the free DNA are boxed and underlined, respectively. 16-nt DNA^{Myc}, DNA minimized to eliminate 5′ and 3′ single-stranded extensions to the G-quadruplex. 16-nt mutant DNA^{Myc}, variant of the former with two mutations (red) to enforce the three quartets observed in the DHX36-DSM–DNA^{Myc} co-crystal structure. **b**, Size-exclusion chromatograms (see Methods) of 22-nt DNA^{Myc}, 16-nt DNA^{Myc} and 16-nt mutant DNA^{Myc} in the presence of either 150 mM or 20 mM KCl, demonstrating greater conformational homogeneity of the DNAs at lower KCl concentration. **c**, DSC thermograms (before buffer correction) for the three DNAs, in 20 mM KCl. Three independent experiments are plotted for each DNA. **d**, Triplicate nonlinear least-squares analyses of thermograms for the three DNAs. Black and red curves, buffer-corrected DSC data and curve-fits, respectively. T_m (melting temperature) and ΔH (enthalpy change) are reported as mean ± s.d. Each experiment was repeated three times with two sets of identical DNA preparations.

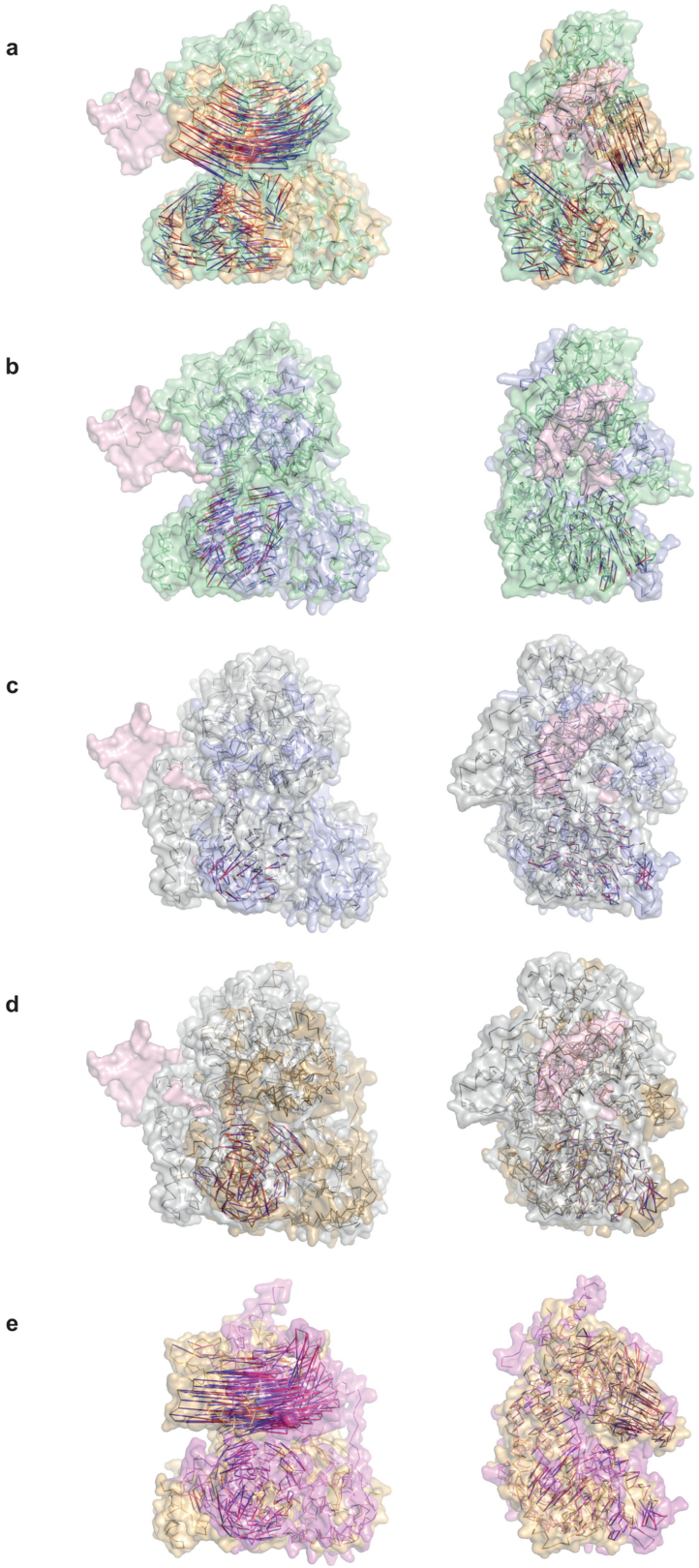

Extended Data Fig. 6 | Alignments of the structures of DHX36, MLE, and Prp43. RecA1 domains were superimposed. Vectors from red to blue denote Cα displacement between identical or structurally homologous residues. **a**, Superposition of DHX36-DSM–DNA^{Myc} and unliganded DHX36-core (5VHA) structures (green and orange, respectively). DNA^{Myc} is pink. **b**, Superposition of DHX36-DSM–DNA^{Myc} (green) and Prp43 (ref. [16]) bound to rU_{16} and ADP•BeF_3^- (5LTA; blue; ground'). DNA^{Myc} from the DHX36-DSM–DNA^{Myc} structure is pink. **c**, Superposition of Prp43 bound to rU_8 and ADP•BeF_3^- (5LTA; blue; 'ground') to MLE[15] bound to rU15 and ADP•AlF_4^- (5AOR; silver; 'transition'). DNA^{Myc} from the DHX36-DSM–DNA^{Myc} structure is pink. **d**, Superposition of MLE bound to rU_{15} and ADP•AlF_4^- (5AOR; silver; 'transition') and Prp43 bound[13,14] to ADP (3KX2/2XAU; gold; 'post-hydrolysis'). DNA^{Myc} from the DHX36-DSM–DNA^{Myc} structure is pink. **e**, Superposition of Prp43 bound to ADP (3KX2/2XAU; gold; 'post-hydrolysis') to unliganded DHX36-core (5VHA; magenta; 'apo').

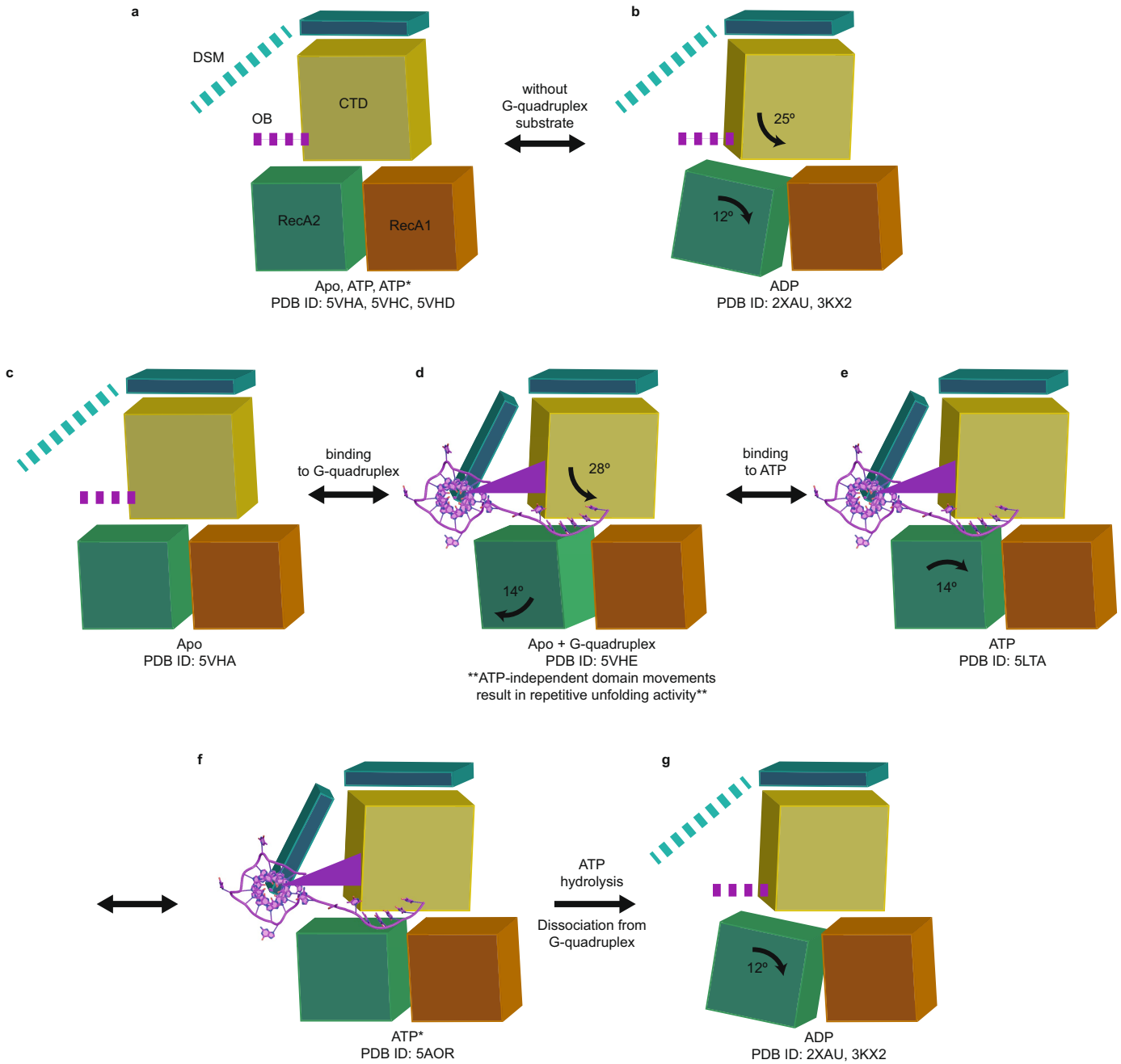

Extended Data Fig. 7 | Model of the mechanochemical cycle of the DEAH/RHA helicase DHX36. The domain motions are based on the superpositions in Extended Data Fig. 6. The orange, green, yellow, and blue blocks represent the RecA1 domain, RecA2 domain, C-terminal domain, and N-terminal extension, respectively. The purple wedge represents the OB domain. Bold dotted lines represent likely intrinsically disordered protein motifs that fold upon G-quadruplex binding. **a**, **b**, In the absence of a G-quadruplex nucleic acid substrate, DHX36 cycles between an apo (or structurally indistinguishable ATP-bound) state and a post-hydrolysis state. **c**, **d**, DHX36 binds the G-quadruplex substrate and pulls on it in the 3′-direction through concerted and opposite rotations of the RecA2 and C-terminal domains. Oscillation of the RecA2 and C-terminal domains is likely to be responsible for the ATP-independent repetitive unfolding activity detected by smFRET[22] (Extended Data Fig. 2 and Fig. 4). **d**, **e**, Binding of ATP induces domain closure. **f**, **g**, ATP hydrolysis yields a post-hydrolysis state that is incompatible with nucleic acid binding. ADP dissociates, and DHX36 is reset back to its apo state (**c**). In addition to the rearrangement of motif Va[17], ATP hydrolysis is stimulated by nucleic acid binding, probably because nucleic acid binding results in the opening of the helicase core. Diffusion into the NTP binding pocket is thus increased. The model in **e** is based on the superposition in Extended Data Fig. 6b. The model in **f** is based on the superposition in Extended Data Fig. 6c. The model in **f** is based on the superposition in Extended Data Fig. 6c. The model in **g** is based on the superposition in Extended Data Fig. 6d.

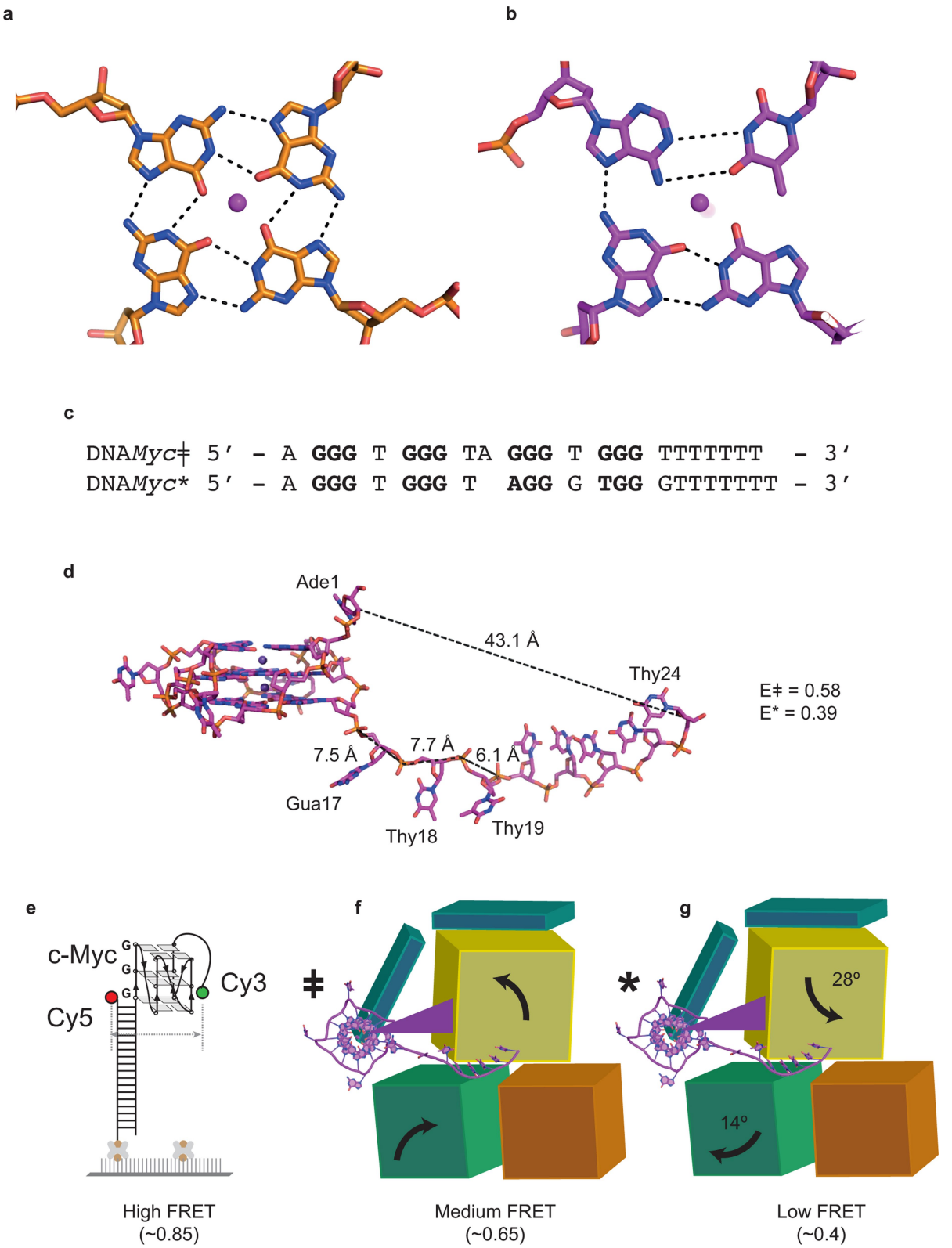

Extended Data Fig. 8 | See next page for caption.

Extended Data Fig. 8 | Comparison of canonical and reorganized DNA^{Myc} G-quadruplex. DNA^{Myc}‡ denotes the canonical DNA^{Myc} structure[20,24] whereas DNA^{Myc}* represents the reorganized DNA^{Myc} found in the DHX36-DSM–DNA^{Myc} co-crystal structure. **a**, Structure of the DNA^{Myc}‡ top G-quartet (PDB ID: 2N21). **b**, Structure of the DNA^{Myc}* top G-quartet. **c**, Primary sequence alignment of the canonical and reorganized DNA^{Myc} G-quadruplex. Bold residues participate in formation of a quartet. **d**, The structure of DNA^{Myc} G-quadruplex found in our co-crystal structure, represented here by DNA^{Myc}*. Distances between A1 and T24 as well as G16 and G17, G17 and T18, and T18 and T19 are indicated. Theoretical FRET efficiencies (E) for DNA^{Myc}‡ and DNA^{Myc}* were calculated using $E = 1/[1 + (r/R_0)^6]$ where $R_0 = 53$ Å for the Cy3–Cy5 pair and r is the distance between Cy3 and Cy5. Since smFRET experiments were performed with a DNA^{Myc} G-quadruplex containing a 3′ ssDNA extension of nine thymines, we added the distance between two thymines to the theoretical FRET efficiency model assuming an average internucleotide distance of 7.1 Å. As the difference between the hypothetical DNA^{Myc}‡ previously solved by NMR and DNA^{Myc}* found in our co-crystal structure is one nucleotide, we modelled r‡ and r* as 50.2 Å and 57.3 Å, respectively. From these parameters, we obtained predicted FRET efficiencies of 0.58 and 0.39 for DNA^{Myc}‡ and DNA^{Myc}*, respectively. These predicted FRET efficiencies closely match the experimental oscillating FRET efficiencies of ~0.6 and ~0.4. **e**, The high FRET state of ~0.85 is observed before DHX36 binding to the DNA^{Myc} G-quadruplex. **f**, DHX36 initially binds to DNA^{Myc}‡ (FRET ~0.6). **g**, Probably owing to ATP-independent C-terminal domain rotations also observed[16] with Prp43p, the DNA^{Myc}, G-quadruplex is partially unwound to DNA^{Myc}* (~0.4). DHX36 then oscillates between DNA^{Myc}* and DNA^{Myc}‡ in an ATP-independent repetitive unfolding activity.

Extended Data Table 1 | Data collection and refinement statistics

	DHX36-DSM-DNA^{Myc} (PDB: 5VHE)	DHX36-Core (PDB: 5VHA)	DHX36-Core-BeF_3^- (PDB: 5VHC)	DHX36-Core-AlF_4^- (PDB: 5VHD)
Data collection				
Space group	$P2_1\,2_1\,2_1$	$P2_1$	$P2_1$	$P2_1$
Cell dimensions				
a, *b*, *c* (Å)	72.5, 79.3, 212.1	61.3, 109.2, 62.4	61.9, 111.5, 63.0	62.0, 112.5, 63.2
α, β, γ (°)	90, 90, 90	90, 112.7, 90	90, 110.7, 90	90, 110.3, 90
Resolution (Å)	39.6-3.8 (3.9-3.8)[a]	39.6-2.2 (2.3-2.2)	37.8-2.5 (2.6-2.5)	46.7-2.6 (2.7-2.6)
R_{merge} (%)	27.5 (168)	8.66 (46.7)	7.52 (25.9)	15.0 (80.0)
$\langle I \rangle / \langle \sigma(I) \rangle$	7.8 (1.3)	18.3 (3.0)	16.9 (3.6)	9.9 (1.2)
$CC_{1/2}$	0.994 (0.486)	0.997 (0.883)	0.996 (0.949)	0.994 (0.646)
Completeness (%)	99.2 (94.0)	99.8 (98.1)	91.5 (87.8)	98.8 (98.2)
Redundancy	9.6 (7.6)	6.5 (6.2)	3.5 (3.4)	5.1 (3.6)
Refinement				
Resolution (Å)	39.6-3.8 (3.9-3.8)	39.6-2.2 (2.3-2.2)	37.8-2.5 (2.6-2.5)	46.7-2.6 (2.6-2.6)
No. reflections	12606 (1153)	37004 (3636)	25665 (2446)	26260 (2612)
R_{work} / R_{free} (%)	23.8/28.0	17.7/21.7	19.4/23.3	17.3/21.3
No. atoms	7202	6477	6318	6266
Protein	6697	6286	6189	6126
DNA	503	0	0	0
Ligand/ion	2	0	32	32
Water	0	180	97	108
Mean *B*-factors (Å^2)	120.9	53.6	60.9	50.1
Protein	118.4	53.8	61.8	50.0
DNA	155.2	N/A	N/A	N/A
Ligand/ion	117.5	N/A	47.2	78.8
Water	N/A	47.3	53.3	45.5
R.m.s. deviations				
Bond lengths (Å)	0.002	0.004	0.002	0.002
Bond angles (°)	0.50	0.75	0.52	0.56
Ramachandran analysis (%)				
Favored	91.2	96.3	97.2	96.8
Allowed	7.5	3.2	2.8	3.2
Disallowed	1.3	0.5	0.0	0.0
Mean coordinate precision (Å)	0.47	0.30	0.32	0.21

[a]Values in parentheses are for highest-resolution shell.
One crystal was used for each of the four data sets.

Extended Data Table 2 | Data collection statistics for DHX36-core-SeMet crystals

	DHX36-Core-SeMet 1	DHX36-Core-SeMet 2	DHX36-Core-SeMet 3	DHX36-Core-SeMet 4	DHX36-Core-SeMet 5	DHX36-Core-SeMet <1,2,3,4,5>
Data collection						
Space group	$P2_1$	$P2_1$	$P2_1$	$P2_1$	$P2_1$	$P2_1$
Cell dimensions						
a, *b*, *c* (Å)	62.6, 115.7, 64.0	62.5, 113.6, 63.8	62.5, 113.4, 63.8	62.4, 113.5, 64.0	62.6, 114.7, 63.9	62.6, 114.7, 63.9
α,β,γ (°)	90, 107.3, 90	90, 108.0, 90	90, 108.0, 90	90, 107.8, 90	90, 107.8, 90	90, 107.8, 90
Resolution (Å)	46.7-3.2 (3.3-3.2)[a]	46.6-3.3 (3.4-3.3)	46.6-3.0 (3.1-3.0)	46.6-2.9 (3.0-2.9)	46.7-3.1 (3.2-3.1)	46.7-3.1 (3.2-3.1)
R_{merge} (%)	17.4 (87.6)	17.4 (94.1)	14.5 (84.8)	14.8 (74.8)	14.4 (81.5)	22.4 (102)
$\langle I \rangle / \langle \sigma(I) \rangle$	10.5 (1.3)	10.8 (1.5)	11.6 (1.2)	11.0 (1.4)	12.1 (1.4)	22.7 (2.1)
$CC_{1/2}$	0.995 (0.643)	0.996 (0.646)	0.997 (0.743)	0.997 (0.745)	0.997 (0.798)	0.999 (0.753)
Completeness (%)	97.5 (80.5)	98.6 (88.6)	92.5 (60.8)	90.6 (51.2)	97.9 (12.1)	98.9 (90.1)
Redundancy	7.0 (5.0)	7.0 (4.9)	6.7 (4.8)	6.7 (4.3)	7.0 (5.0)	31.1 (15.5)

[a]Values in parentheses are for highest-resolution shell.
One crystal was used for each of the first five data sets. The last data set resulted from merging all five data sets.

nature research

Corresponding author(s): Adrian R. Ferré-D'Amaré

☐ Initial submission ☐ Revised version ☒ Final submission

Life Sciences Reporting Summary

Nature Research wishes to improve the reproducibility of the work that we publish. This form is intended for publication with all accepted life science papers and provides structure for consistency and transparency in reporting. Every life science submission will use this form; some list items might not apply to an individual manuscript, but all fields must be completed for clarity.

For further information on the points included in this form, see Reporting Life Sciences Research. For further information on Nature Research policies, including our data availability policy, see Authors & Referees and the Editorial Policy Checklist.

Experimental design

1. Sample size

Describe how sample size was determined.

In smFRET experiments, each measurement consists of at least 10,000 molecules. No statistical methods were used to predetermine sample size.

2. Data exclusions

Describe any data exclusions.

No data was excluded.

3. Replication

Describe whether the experimental findings were reliably reproduced.

Reproducibility of findings was established by (1) performing crystallization protocol multiple times to ensure repeatability of crystallization conditions and (2) smFRET experiments were conducted with large sample sizes (>10K molecules) over several experiments to ensure repeatability of smFRET traces and FRET histograms. Attempts at replication yielded similar results for each experiment.

4. Randomization

Describe how samples/organisms/participants were allocated into experimental groups.

Representative FRET traces were chosen based on how closely the the individual molecule displayed representative dwell times between medium and low FRET states. Molecules were chosen that closely matched median dwell times as seen in Ext Data Fig 2e.

5. Blinding

Describe whether the investigators were blinded to group allocation during data collection and/or analysis.

Data blinding is not relevant to this investigation as experiments did not involve clinical trials or screens for efficacy.

Note: all studies involving animals and/or human research participants must disclose whether blinding and randomization were used.

6. Statistical parameters

For all figures and tables that use statistical methods, confirm that the following items are present in relevant figure legends (or in the Methods section if additional space is needed).

n/a	Confirmed	
☐	☒	The exact sample size (*n*) for each experimental group/condition, given as a discrete number and unit of measurement (animals, litters, cultures, etc.)
☐	☒	A description of how samples were collected, noting whether measurements were taken from distinct samples or whether the same sample was measured repeatedly
☐	☒	A statement indicating how many times each experiment was replicated
☒	☐	The statistical test(s) used and whether they are one- or two-sided (note: only common tests should be described solely by name; more complex techniques should be described in the Methods section)
☒	☐	A description of any assumptions or corrections, such as an adjustment for multiple comparisons
☒	☐	The test results (e.g. *P* values) given as exact values whenever possible and with confidence intervals noted
☐	☒	A clear description of statistics including central tendency (e.g. median, mean) and variation (e.g. standard deviation, interquartile range)
☐	☒	Clearly defined error bars

See the web collection on statistics for biologists for further resources and guidance.

Software

Policy information about availability of computer code

7. Software

Describe the software used to analyze the data in this study.	HKL-2000, PHENIX (Version 1.10.1_2155), and Coot (0.8-pre EL revision 5121) were used to analyze crystallographic data in this study. RESOLVE and PHASER utilized in this study are part of the PHENIX platform. Thermograms were analyzed with OriginLab. Structures were visualized by Pymol and Chimera. smFRET data acquisition and analysis software from CPLC (https://cplc.illinois.edu/software/) was used to analyze smFRET data.

For manuscripts utilizing custom algorithms or software that are central to the paper but not yet described in the published literature, software must be made available to editors and reviewers upon request. We strongly encourage code deposition in a community repository (e.g. GitHub). *Nature Methods* guidance for providing algorithms and software for publication provides further information on this topic.

Materials and reagents

Policy information about availability of materials

8. Materials availability

Indicate whether there are restrictions on availability of unique materials or if these materials are only available for distribution by a for-profit company.	No unique materials were used.

9. Antibodies

Describe the antibodies used and how they were validated for use in the system under study (i.e. assay and species).	No antibodies were used.

10. Eukaryotic cell lines

a. State the source of each eukaryotic cell line used.	No eukaryotic cell lines were used.
b. Describe the method of cell line authentication used.	No eukaryotic cell lines were used.
c. Report whether the cell lines were tested for mycoplasma contamination.	No eukaryotic cell lines were used.
d. If any of the cell lines used are listed in the database of commonly misidentified cell lines maintained by ICLAC, provide a scientific rationale for their use.	No commonly misidentified cell lines were used.

Animals and human research participants

Policy information about studies involving animals; when reporting animal research, follow the ARRIVE guidelines

11. Description of research animals

Provide details on animals and/or animal-derived materials used in the study.	No animals were used.

Policy information about studies involving human research participants

12. Description of human research participants

Describe the covariate-relevant population characteristics of the human research participants.	This study did not involve human participants.